Single-photon imaging system with a fiber optic taper*

ZHENG Tian-xiang (郑天翔)[1], **SHEN Guang-yue** (申光跃)[1], **LI Zhao-hui** (李召辉)[1], **WU E** (武愕)[1,2], **CHEN Xiu-liang** (陈修亮)[1]**, **and WU Guang** (吴光)[1,2]

1. State Key Laboratory of Precision Spectroscopy, East China Normal University, Shanghai 200062, China

2. Collaborative Innovation Center of Extreme Optics, Shanxi University, Taiyuan 030006, China

(Received 10 February 2018; Revised 2 April 2018)

©Tianjin University of Technology and Springer-Verlag GmbH Germany, part of Springer Nature 2018

We report a time-of-flight photon-counting imaging system in conjunction with a single-photon detector mounted with a fiber optic taper, which equivalently enlarges the active area of the single-photon detector by 100 times. The field of view of the imaging system is extended from ±0.57° to ±7° by using the fiber optic taper to collect the scattered photons. Since only a single avalanche photodiode is used, the noise level of the system is maintained at a low level. We demonstrate the scanning of the targets at a stand-off distance of 28 m with a centimeter depth resolution.

Document code: A **Article ID:** 1673-1905(2018)04-0267-4

DOI https://doi.org/10.1007/s11801-018-8024-y

Time-of-flight (TOF) laser ranging and imaging has been widely used in remote sensing such as driverless vehicle[1], 3D mapping the city[2], underwater imaging[3], topography[4-6], and canopy height detection[7]. In comparison with conventional TOF laser ranging systems in which high-power pulsed lasers are utilized for the long-distance ranging of non-cooperative targets, the techniques of single-photon detection and time-correlated single-photon counting (TCSPC) remarkably decrease the power consumption for the long-distance ranging and imaging by improving the detection sensitivity to the quantum limit in the photon-counting laser ranging systems[8-15]. A data cloud should be formed by analyzing each point in the depth image. As the targets are illuminated with a laser beam of large divergence angle, and the scattered photons are detected by Geiger-mode avalanche photodiode (APD) arrays[16], the non-scanning 3D laser imaging system is quite simple and robust. However, the system noise induced by the arrays of the APD deteriorates the performance of the system. When it comes to the scanning systems, a collimated laser beam and a single-element detector are used to improve the optical signal-to-background ratio. The active areas of the APD-based single-photon detectors are commonly designed to be quite small, especially for the infrared region, so as to reduce the noise. Yet the field of view (FOV) is limited by the size of the active area of the detector. Ref.[17] proposed a co-axial scanning technique which realized the kilometer-range depth imaging by employing a near-infrared single-photon detector with small active area, and the reported FOV is about ±2.5°. Although it is simple to enlarge the FOV of the system by using a static detector of larger active area[16], the noise remains a non-neglected issue.

In this paper, we demonstrate a photon-counting laser imaging system with collimated scanning laser beam and a static single-photon detector of Geiger-mode Si-APD mounted with a fiber optic taper[18]. Compared with the system without the fiber optic taper, the FOV of the system is extended from ±0.57º to ±7º with a single-photon detector whose active area is about 0.2 cm^2. The system achieves 210 pixels×270 pixels 3D photon-counting laser imaging.

The setup of the photon-counting laser imaging system with a fiber optic taper is shown in Fig.1. A 532-nm pulsed laser source is used. The repetition frequency of the laser is set to 1 kHz while the pulse width is less than 1 ns. A beam expander (BE) is designed to decrease the divergence angle of the laser beam to around 0.3 mrads. Travelling through the BE, the diameter of the beam spot is around 10 mm within a range of 30 m, guaranteeing spatial resolution of the image. At the output of the BE, the laser beam is split into two parts by a beam splitter (BS). One part of the laser beam is detected by a PIN photodiode and used as the start trigger of the TCSPC module, and the other is transmitted to the target. The scanning angle of the output laser beam is controlled by a pair of galvanometer scan mirrors (GM) at *X* axis and *Y* axis, and the average power of the output laser beam after the GM is 320 μW. The sizes of the GM used in this experiment are 1.2 cm^2 and 1.5 cm^2 of the *X* axis and *Y* axis, respectively. Considering the inherent nonlinear relationship between the deflection angles and the corresponding *X*-*Y* coordinates, the pillow-shaped distortion

* This work has been supported by the National Natural Science Foundation of China (Nos.11774095, 11374105, 61378033 and 11621404), the Program of Introducing Talents of Discipline to Universities (No.B12024), the Shanghai International Cooperation Project (No.16520710600), and the Shuguang Program by Shanghai Education Development Foundation and Shanghai Municipal Education Commission (No.15SG22).

** E-mail: xlchen@phy.ecnu.edu.cn

would be taken into account. The distortion ratio in our experiment is 0.13%, which can be neglected. To characterize the system, a model of horse is used as a target at a stand-off distance of 28 m.

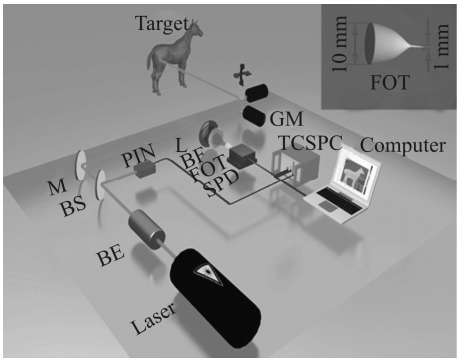

BE: beam expander; M: mirror; BS: beam splitter; GM: galvanometer scan mirrors; L: lens; BF: bandpass filter; FOT: fiber optic taper; SPD: single-photon detector; TCSPC: time-correlated single-photon counting module

Fig.1 Schematic of the photon-counting laser imaging system (Inset shows the structure of the FOT with the large and small faceplates of 10 mm and 1 mm in diameter, respectively.)

The scattered photons from the target are collected and focused by a lens (L). The beam spot moves in the focal plane when the laser scans. The moving range of the beam spot depends on the focal length of the L. The focal length and the diameter of L in this experiment are both 25.4 mm. Unlike the co-axial system where the transmit and receive channels share the same optical path, leading to the serious backward scattering noise generated by the components in the system[17], the noise is mainly from the background without the influence from the transmit channel in the off-axis system. In our experiment, a 1-nm narrow bandpass filter (BF) with a central wavelength at 532 nm is used to reduce the background noise. A fiber optic taper (FOT) is placed between the lens L and the single-photon detector. The large faceplate of the fiber optic taper is on the focal plane of L while the small faceplate is coupled to the active area of the single-photon detector. The FOT is a commercial gradual taper manufactured via the fused biconical taper process. The length and the taper angle are 20 mm and 48.5°, respectively. The demagnification ratio of the taper determines the FOV of the single-photon imaging system. Larger ratio leads to larger FOV. Meanwhile, the integration time for the scattering photon counting depends on the transmittance of the FOT. Higher transmittance leads to shorter integration time. Considering the manufacturing imperfectness of the FOT, in our experiment, the optimized demagnification ratio of the fiber optic taper is set to be 10:1, and the average transmittance of the FOT is about 27%. The sizes of the large faceplate and the small faceplate are 10 mm and 1 mm in diameter, respectively. Due to the fiber optic taper, the active area of the single-photon detector is equivalently enlarged by 100 times, which leads to a larger FOV of the imaging system. The average transmittance of the FOT is measured by coupling a 532-nm laser to the large faceplate of the taper and monitor the laser power at the small faceplate. As shown in Fig.2, the fluctuation of the photon counts between the scanning angle ±7º shows that the transmittance is not uniform, and the standard deviation of the normalized photon counts between the effective scanning angle (±7º) is 2.7%. In the single-photon counting imaging system, the TOF of the scattered photons is recorded by looking for the correlated photon count peaks in the TCSPC. Therefore, the transmittance homogeneity would not affect the quality of the image unless the noise of the system is almost the same as the scattered photon counts within the selected time bin. The scanning angle of the system without the fiber optic taper is about ±0.57º according to

$$\theta = \arctan(\frac{r}{f}), \tag{1}$$

where θ is the scanning angle, r is the radius of the active area, and f is the focal length of the L. As the X axis of the presented system shares the same structure with that of the Y axis, the maximum scanning angle at X axis is identical to that at Y axis. In order to estimate the scanning capability of the imaging system, we scan the GM at X axis, and record the photon counts at corresponding angles with integration time of 0.5 s for each angle acquisition. The full FOV of the system with FOT could achieve ±7º, while the FOV is less than ±1º without FOT.

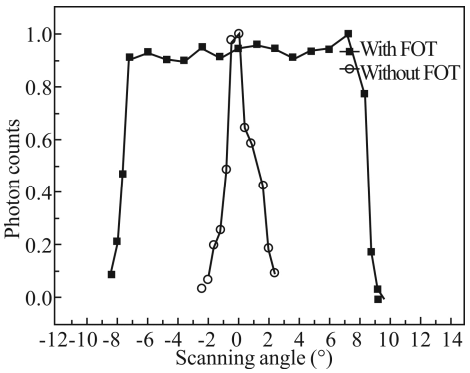

Fig.2 Photon counts as a function of the scanning angle with and without FOT

We perform the indoor trial to investigate the acquisition of depth images from scenes containing several non-cooperative targets such as the security door, the wall, the model of horse and the optical table as shown in Fig.3(a). The security door is about 30.1 m away from the system, and the model of horse is about 1.7 m away from the security door. The table is 3.9 m in front of the horse. To distinguish the targets clearly, a security door and a part of the wall at a stand-off distance of 30 m are used as the backplanes, which also provide a rough calibration of the image in X-Y dimension. Limited by the

width of the laboratory corridor, the scanning angle of the trial is set to about ±3.7°.

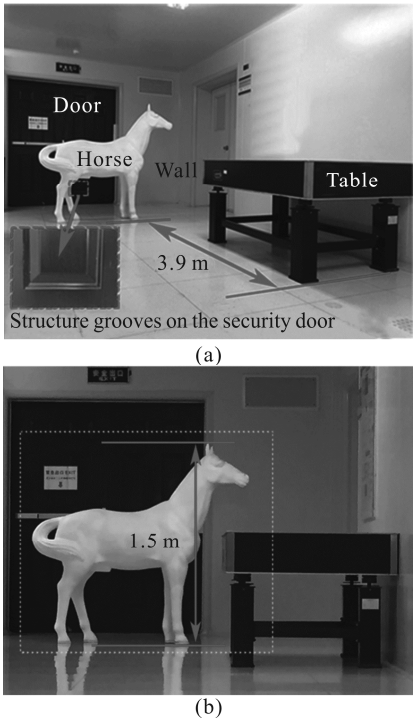

Fig.3 (a) Photo of the scanning area including a horse model, a security door, a wall and an optical table (Inset: structure grooves on the security door); (b) Photo of the horse model (The area in the box is the close-up picture of the scene scanned.)

As shown in Fig.3(b), the height of the horse model is 1.5 m. The model is made of white plastics. The single-photon detector used in this system is a Geiger-mode Si-APD, and the detection efficiency of the detector at the selected wavelength of 532 nm is around 24%, while the dark count rate is about 12×10^3 counts per second. The captured image of the scanned scene using 210 pixels×270 pixels is shown in Fig.4(a), while the color bar scales the different distance. The acquisition time of the experiment is limited to 0.1 s per pixel consequently. The image in Fig.4(a) corresponding to the box in Fig.3(b) can be separated into three layers. The first layer includes the security door and the wall, which is the farthest from the system. The nearest one is the surface of the optical table. In between is the image of the horse model. The jitter of the system is around 1 ns full width at half maximum and the precision is about 15 mm. The two ears of the horse model are respectively distinguished and the heaving chest is apparently revealed by different colors in Fig.4(a). Fig.4(b) shows the depth plot from another perspective. It is clear that the area beneath the body of the horse model shows the structure grooves on the security door, and the edge of the table is obvious. However, there are lots of noises around the optical table. Fig.4(c) shows the noise around the table existing at almost the same depth as the optical table, which indicates that the noise may be caused by the stray lights around the laser beam. The central spot of the laser beam is about 1 cm, but there are stray lights around the central spot. The program we use would only pick the highest peak in the TOF curve. If the photon intensity from the optical table by the stray lights is stronger than that from the wall, the program would take the signal from the optical table as the target depth information. Unlike the noise around the optical table, there are much less noises around the house model, and the outline of the horse model is quite clear. As the distance between the horse model and the security door is close enough, the signal from the door would stronger than the stray noise signal from the horse model and would not be confused. In Fig.4(d), both the legs and the ears of the horse model present the depth differences.

In the glancing angle scanning situation, the noise is easily produced which would blur the edge of the image. In our experiment, the structure grooves on the security door are hard to be observed in the elevation view. As shown in Fig.4(a), the area above the horse model becomes blurry in the image because of the noise from the structure grooves on the security door. Thus, it is necessary to wipe off the noise to acquire a clear image. By comparing the measured distances of four neighbor pixels, if the difference of the distance between the processing pixel and the neighbor pixel is beyond the threshold, this pixel would be picked out as a noise and replaced by the average value of the four neighbor pixels. To wipe off the noise completely, the program is implemented twice and the result is shown in Fig.5. Due to the high resolution of the image, this method doesn't blur the detail of the image. With the removal of the noise, the image becomes clearer, especially the area above the horse model. Compared with Fig.4(a), the structure grooves on the security door are more distinct.

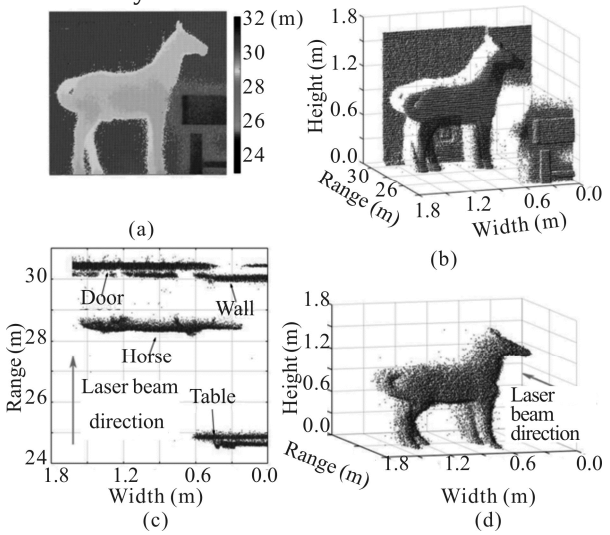

Fig.4 (a) Elevation view image with color bar of the scene scanned (The scan covers a region of approximately 140 cm×180 cm using 210 pixels×270 pixels, resulting in a pixel-to-pixel spacing of approximately 6 mm in both scanning directions.); (b) Surface profile plot of the scanned scene from another perspective; (c) Top view image of the scene; (d) Depth plot of the horse model

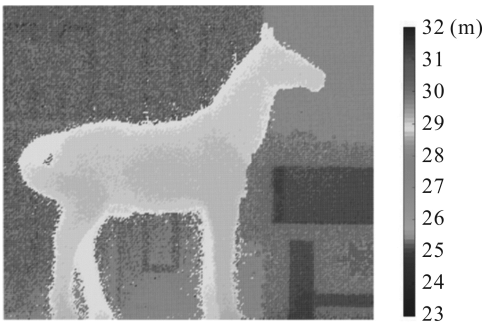

Fig.5 Corrected elevation view image of the scanned scene

In conclusion, we demonstrate a TOF imaging system with a fiber optic taper. The fiber optic taper is able to shrink the image from the large faceplate to the small faceplate without distortion, which doesn't affect the property of the depth imaging. The FOV of the laser imaging system is enlarged from ±0.57º to ±7º, with the single-photon detector's active area of 0.2 cm^2. This system paves the way of the construction of the depth imaging system with larger FOV and low noise for applications in the airborne and shipboard underwater imaging device, where the weight of the system is strictly controlled.

References

[1] A. Broggi, P. Grisleri and P. Zani, Sensors Technologies for Intelligent Vehicles Perception Systems: A Comparison between Vision and 3D-LIDAR, in 16th International IEEE Conference on Intelligent Transportation Systems, 887 (2013).

[2] B. Schwarz, Nat. Photonics **4**, 429 (2010).

[3] A. Halimi, A. Maccarone, A. McCarthy, S. McLaughlin and G. S. Buller, IEEE Transactions on Computational Imaging **3**, 472 (2017).

[4] P. Tarolli, Geomorphology **216**, 295 (2014).

[5] D. E. Smith, M. T. Zuber, G. B. Jackson, J. F. Cavanaugh, G. A. Neumann, H. Riris, X. Sun, R. S. Zellar, C. Coltharp, J. Connelly, R. B. Katz, I. Kleyner, P. Liiva, A. Matuszeski, E. M. Mazarico, J. F. McGarry, A.-M. Novo-Gradac, M. N. Ott, C. Peters, L. A. Ramos-Izquierdo, L. Ramsey, D. D. Rowlands, S. Schmidt, V. S. Scott, G. B. Shaw, J. C. Smith, J.-P. Swinski, M. H. Torrence, G. Unger, A. W. Yu and T. W. Zagwodzki, Space Sci. Rev. **150**, 209 (2010).

[6] A. Swatantran, H. Tang, T. Barrett, P. DeCola and R. Dubayah, Sci. Rep. **6**, 28277 (2016).

[7] M. S. Moussavi, W. Abdalati, T. Scambos and A. Neuenschwander, Int. J. Remote Sens. **35**, 5263 (2014).

[8] H. Peng, Y. Wang, W. Meng, P. Yan, Z. Li, C. Li, H. Pan and G. Wu, Optoelectronics Letters **14**, 129 (2018).

[9] R. Tobin, A. Halimi, A. McCarthy, X. Ren, K. J. McEwan, S. McLaughlin and G. S. Buller, Optical Engineering **57**, 031303 (2017).

[10] M. Henriksson, H. Larsson, C. Grönwall and G. Tolt, Optical Engineering **56**, 031204 (2016).

[11] A. M. Pawlikowska, A. Halimi, R. A. Lamb and G. S. Buller, Optics Express **25**, 11919 (2017).

[12] Y. Liang, J. Huang, M. Ren, B. Feng, X. Chen, E. Wu, G. Wu and H. Zeng, Opt. Express **22**, 4662 (2014).

[13] A. Maccarone, A. McCarthy, X. Ren, R. E. Warburton, A. M. Wallace, J. Moffat, Y. Petillot and G. S. Buller, Opt. Express **23**, 33911 (2015).

[14] Z. Li, E. Wu, C. Pang, B. Du, Y. Tao, H. Peng, H. Zeng and G. Wu, Opt. Express **25**, 10189 (2017).

[15] S. Jahromi, J. P. Jansson and J. Kostamovaara, Opt. Express **24**, 21619 (2016).

[16] C. Niclass, M. Soga, H. Matsubara, S. Kato and M. Kagami, IEEE Journal of Solid-State Circuits **48**, 559 (2013).

[17] A. McCarthy, X. Ren, A. Della Frera, Nathan R. Gemmell, N. J. Krichel, C. Scarcella, A. Ruggeri, A. Tosi and G. S. Buller, Opt. Express **21**, 22098 (2013).

[18] C.I. Coleman, Advances in Electronics and Electron Physics **64**, 649 (1985).